


Topologically protected wave packets and quantum rings in silicene

Bartłomiej Szafran , Bartłomiej Rzeszotarski, and Alina Mreńca-Kolasińska

AGH University of Science and Technology, Faculty of Physics and Applied Computer Science, al. Mickiewicza 30, 30-059 Kraków, Poland



(Received 20 May 2019; revised manuscript received 22 July 2019; published 22 August 2019)

We study chiral wave packets moving along the zero line of a symmetry-breaking potential of vertical electric field in buckled silicene using an atomistic tight-binding approach with initial conditions set by an analytical solution of the Dirac equation. We demonstrate that the wave packet moves with a constant untrembling velocity and with a preserved shape along the zero line. Backscattering by the edge of the crystal is observed that appears with the transition of the packet from K to K' valley or vice versa. We propose a potential profile that splits the wave packet and next produces interference of the split parts that acts as a quantum ring. The transition time exhibits Aharonov-Bohm oscillations in the external magnetic field that are translated to conductance oscillations when the intervalley scattering is present within the ring. We study wave packet dynamics as function of the width of the packet up to the limit of plane waves. In the stationary transport limit the conductance oscillation period is doubled and the scattering density oscillates between the left and right arms of the ring as function of the magnetic field. We demonstrate that this effect is also found in a quantum ring defined by the zero lines of the symmetry-breaking potential in bilayer graphene.

DOI: [10.1103/PhysRevB.100.085306](https://doi.org/10.1103/PhysRevB.100.085306)

I. INTRODUCTION

In monolayer honeycomb materials, including graphene [1], Xenes [2] (silicene [3,4], germanene [4,5], stanene [6]), transition metal dichalcogenides [7], or bismuthene [8], the Fermi level appears in two nonequivalent valleys of the Brillouin zone. In graphene ribbons [9] with zigzag edges there is a strict correspondence between the valley state and the direction of the current flow [10–12]. The valley protects the chiral [13] electron transport from backscattering by long-range potential disorder, which led to the valley electronics [14,15] or application of the valley degree of freedom to information processing [15–17].

In bilayer [18] and staggered monolayer graphene [19] a topological confinement inside the sample, far from the edges, was found [18,19] along a zero line of inversion-symmetry-breaking potential. For bilayer graphene [20] this potential is introduced by an electric field perpendicular to the layers [18]. The bias opens the energy gap in the band structure [20,21]. For an inhomogeneous electric field that is inverted at the zero line in space, topologically protected chiral currents have been found [18] confined in space to a region of the electric field flip. The flip line provides a one-dimensional confinement or quantum-wire-type channels [22–25]. The one-dimensional confinement of currents is also found in the quantum Hall conditions at the n-p junctions [26] induced by electric fields. In contrast to the currents localized at the n-p interface [27–29], the confinement in zero-line channels does not require external magnetic field [18]. Note that formation of an energy gap was also found in epitaxial monolayer graphene due to the sublattice symmetry breaking by the substrate [30]. However, the gap of this origin cannot be easily inverted for the topological confinement.

A perpendicular electric field opens the energy gap for the buckled Xenes monolayers [2,31,32], and an inversion of the

field induces topological confinement similarly as in bilayer graphene [33]. In contrast to bilayer graphene, (i) in Xenes the chiral energy level that passes from the valence to the conduction band is a linear function of the wave vector. In Xenes a (ii) single topological state per current direction is present instead of two as in bilayer graphene. As a consequence of (i) and (ii) the wave packet formed at zero line in Xenes should be stable against excitations and should travel with a constant shape due to independence of the velocity on the wave vector.

In this paper we study the dynamics of the chiral wave packets along the zero lines of the electric field in silicene [2,34–39], the Xenes material for which the gating technology is the most advanced, with a successful application for the field effect transistor [40]. We find that the chiral wave packets move with the Fermi velocity and the motion of the topological packets is free from Zitterbewegung [41–44], which is characteristic to the solution of the Dirac equation and is found also for Weyl fermions in graphene [42,43,45]. Moreover, the topological electron packets move with a constant shape, similarly to solitons, that in other conditions require interaction with the environment—see the electron solitons self-focused with interaction to the metal gates in heterostructures [46] or the Trojan wave packets formed by carefully prepared electromagnetic field [47,48].

We show that the chiral electron packets can be transferred from one valley to the other by backscattering from the edge of the crystal and we find that the packet appears in the opposite valley in a restored shape. Potential profiles that act as beam splitters and quantum rings [49] are proposed. An interference of the split parts of the wave packet can be controlled by external magnetic field threading the quantum ring. The ring stores the wave packet for a time that is a periodic function with the period the flux quantum. The Aharonov-Bohm [50] conductance oscillations are also demonstrated for the system with an intervalley scattering present. The

topological rings are a new form of quantum rings for Dirac electrons, with respect to previously considered systems with structural confinement [51–55], mass confinement [56–58] or the confinement at circular n-p junctions in the quantum Hall conditions [59].

In the long wave packet limit, i.e., when the width of the packet is comparable with the diameter of the ring, the interference within the ring is translated into an imbalance of the scattering density in the left and right arms of the ring that becomes a periodic function with doubled Aharonov-Bohm period. The result is also found in the stationary transport for silicene and bilayer graphene.

This paper is organized as follows. In Sec. II we provide an analytic solution to the Dirac equation for the topologically protected currents at the inversion of the electric field (Sec. II A). In Sec. II B the solution of the continuum approximation (Sec. II A) is translated to atomistic tight-binding description which naturally accounts for the intervalley scattering, and the time stepping procedure is explained. In the Sec. III we test the stability of the wave packet against the intervalley transition (Sec. III A) and describe the Aharonov-Bohm [50] oscillations of the electron storage time by the ring (Sec. III B). Section III C describes the conductance oscillations for intervalley scattering within the ring. The long wave packet limit is discussed in Sec. III D, and the limit is confronted with the standard calculation based on the stationary electron scattering in Sec. III E. Section III F shows the results of the Landauer approach for quantum rings defined by the zero lines in bilayer graphene. Section IV contains the summary.

II. THEORY

A. Chiral currents confined by the energy gap inversion

The chiral currents at the band inversion in silicene similar to the ones in bilayer graphene [18] were found in Ref. [33]. For buckled monolayers as well as for bilayer systems the energy gap can be tailored in space using multiple split gates with inverted polarization. The idea of the local manipulation of the energy gap by dual split gates was proposed for topological confinement [18] and pseudospin electronics in bilayer systems [60–62].

Here, we consider a buckled silicene monolayer sandwiched in between top and bottom gates [Figs. 1(a) and 1(b)]. The gates are split, so that the electric field changes orientation along the y axis (i.e., for $x = 0$). We model the potential at the A sublattice using an arctangent function,

$$V_A(x) = \frac{2V_g \arctan(x/\lambda)}{\pi}. \quad (1)$$

We assume that the silicene is embedded symmetrically between the gates, so that on the B sublattice we have $V_B(x) = -V_A(x)$ [Fig. 1(c)]. The potential bias between the sublattices opens an energy gap in the band structure [31,32]. For potential of Eq. (1) the energy gap is inverted at $x = 0$ by the flip of the electric field orientation.

For the wave function components defined on sublattices $\psi = (\psi_A, \psi_B)^T$ the low-energy approximation to the atomistic tight-binding Hamiltonian reads [33]

$$H_\eta = \hbar v_F (k_x \tau_x - \eta k_y \tau_y) + V(\mathbf{r}) \tau_z - \eta \tau_z \sigma_z t_{SO}, \quad (2)$$

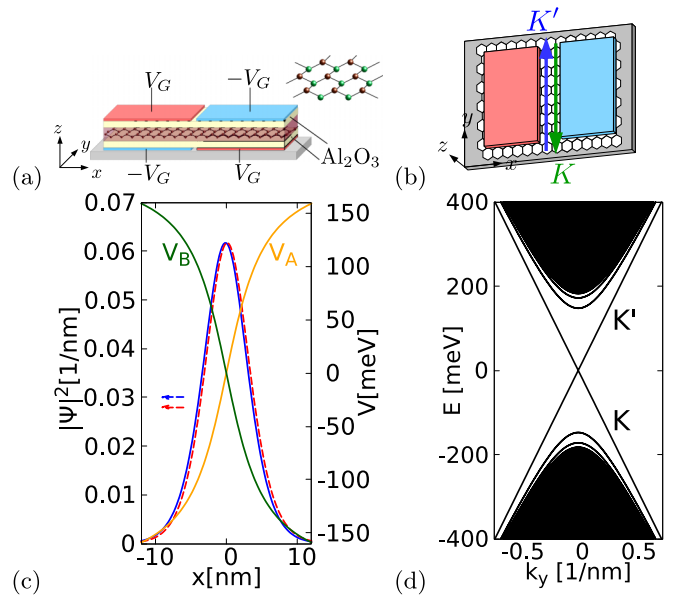


FIG. 1. (a) Schematic side view of a silicene monolayer embedded in a dielectric sandwiched between top and bottom gates with the A sublattice on top (red dots in the inset) closer to a positively $V_G > 0$ biased top gate (red color) gated inducing a negative potential energy for $x < 0$. (b) Top view of the system. The K' (K) valley current flows leaving the negative (positive) potential energy on the A sublattice on the left hand side. The flake has a zigzag (armchair) termination at the edges with constant y (x). (c) The potential profile on the A and B sublattices (right axis) and the wave function on the A sublattice as calculated in the continuum approximation [Eq. (6)]. The blue solid (red dashed) lines show the wave functions with the positive (negative) product of the valley index η and the spin σ_z eigenvalue for $\lambda = 4$ nm and $V_g = 0.2$ eV. (d) The dispersion relation calculated numerically.

where η is the valley index ($\eta = 1$ for the K valley and -1 for the K' valley), τ_x , τ_y , and τ_z are the Pauli matrices in the sublattice space, $\mathbf{k} = -i\nabla$, the Fermi velocity v_F is determined by the nearest distance between Si atoms $d = 2.25$ Å and the tight-binding hopping parameter $t = 1.6$ eV [4,36], $v_F = 3dt/2\hbar$. In Eq. (2) $t_{SO} = 3.9$ meV is the intrinsic spin-orbit coupling constant [4,36]. The intrinsic spin-orbit coupling is diagonal in the basis of eigenstates of the z component of the spin and $\sigma_z = \pm 1$ is treated as a quantum number.

With potential given by Eq. (1) the Hamiltonian commutes with the $\frac{\partial}{\partial y}$ operator. The common eigenfunctions of the energy and y momentum component can be put in form $\psi^{k_y}(x, y) = \exp(ik_y y) [\psi_A^{k_y}(x) \ \psi_B^{k_y}(x)]^T$. The Hamiltonian eigenfunctions fulfill the system of equations

$$\frac{[V_A(x) - E - \eta \sigma_z t_{SO}] \Psi_A(x)}{i\hbar v_F} = (\Psi'_B - \eta k_y \Psi_B), \quad (3)$$

$$\frac{[-V_A(x) - E + \eta \sigma_z t_{SO}] \Psi_B(x)}{i\hbar v_F} = (\Psi'_A + \eta k_y \Psi_A), \quad (4)$$

where the prime stands for x derivative. We plug in Eqs. (3) and (4) a relation $\Psi_B = i\Psi_A$, i.e., a guess based on a numerical solution that allows us to derive an analytical solution for states localized near the zero-line area. A sum of the resulting

equations relates the potential and the wave function

$$V_A(x) - \eta\sigma_z t_{\text{SO}} = -\hbar v_F \frac{\partial}{\partial x} \ln \Psi_A(x). \quad (5)$$

For the specific form of potential given by Eq. (1) the (un-normalized) wave function is found by a standard integration technique

$$\Psi_A = (\lambda^2 + x^2)^{\frac{\lambda V_g}{\pi \hbar v_F}} e^{-\frac{2V_g x}{\pi \hbar v_F} \arctan \frac{x}{\lambda} + \frac{\eta \sigma_z t_{\text{SO}} x}{\hbar v_F}}. \quad (6)$$

The term $x \arctan(x/\lambda)$ in the exponent for low x introduces a Gaussian-like dependence to the wave function and keeps it localized near the band inversion area [Fig. 1(c)]. The average value of $\langle x^2 \rangle^{1/2}$ for $\lambda = 1, 2, 4, 12,$ and 20 nm is 2.45, 2.87, 3.55, 5.45, and 6.83 nm, respectively. In presence of the spin-orbit coupling the wave function is not ideally symmetric with respect to the center of the gap inversion line: the term including the spin-orbit coupling shifts the wave function at left (right) of the inversion line for negative (positive) product of valley index η and the σ_z eigenvalue. For the applied parameters these shifts are not very strong – see the blue and red lines in Fig. 1(c). In the calculations below we set $\sigma_z = 1$.

The energy of the states localized at the gap inversion can be calculated by adding Eqs. (3) and (4) still with the relation $\Psi_B = i\Psi_A$, which gives

$$E = -\eta \hbar k_y v_F. \quad (7)$$

The entire dispersion relation calculated numerically with a finite difference approach [63] is given in Fig. 1(d). The linear band energy is independent of the V_g or λ which only affect the transverse wave function localization at the energy gap inversion line. Above the energy gap a continuous spectrum is found with a parabolic in k_y . Near the zero energy only the localized reflectionless currents flow, and for $V_g = 200$ meV, the gap is wide enough to make the currents stable at room temperature. For the Fermi wave vector $k_F \simeq 0.25$ nm⁻¹ ($E_F \simeq 100$ meV) the continuum appears still 100 meV above the linear band.

The sign of the electron velocity within the linear band $v(k_y) = \frac{1}{\hbar} dE/dk_y = -\eta v_F$ depends on the valley index. Hence, the transport at the inversion line is chiral, i.e., the electron states of the valley K' (K) go up (down) along the electric field flip line [Fig. 1(b)]. Generally, in the states localized along the field flip the current in the K' (K) valley flows with the negative (positive) potential at the A sublattice at the left-hand side.

B. Chiral wave packets in the atomistic tight-binding approach

1. Atomistic Hamiltonian

Since the electron velocity in the linear chiral band is independent of k_y , the wave packet localized at the flip of the electric field should move with an unchanged shape along the $x = 0$ line. The description of the electron wave packets stabilized by the valley degree of freedom calls for an approach that takes into account the intervalley scattering. A natural choice is the atomistic tight-binding approach. The positions of the ions of the A sublattice $\mathbf{r}_m^A = m_1 \mathbf{a}_1 + m_2 \mathbf{a}_2$ are generated with the crystal lattice vectors $\mathbf{a}_1 = a(\frac{1}{2}, \frac{\sqrt{3}}{2}, 0)$ and $\mathbf{a}_2 = a(1, 0, 0)$, where $a = 3.89$ Å is the silicene lattice

constant, and m_1, m_2 are integers. The B sublattice ions are generated by $\mathbf{r}_m^B = \mathbf{r}_m^A + (0, d, \delta)$, with the vertical shift of the sublattices $\delta = 0.46$ Å. The coordinates of the center of the valleys in the reciprocal space are $\mathbf{K}_\eta = (\frac{4\pi\eta}{3a}, 0)$ [35]. The valleys for $\eta = 1$ (-1) are referred to as K (K').

We use the Hamiltonian [34,36,64]

$$H_{TB} = -t \sum_{\langle m,l \rangle} p_{ml} c_m^\dagger c_l + it_{\text{SO}} \sigma_z \sum_{\langle\langle m,l \rangle\rangle} p_{ml} v_{ml} c_m^\dagger c_l + \sum_m V(\mathbf{r}_m) c_m^\dagger c_m + \frac{g\mu_B B}{2} \sigma_z, \quad (8)$$

where $\langle m, l \rangle$ stands for the nearest-neighbor ions, $\langle\langle m, l \rangle\rangle$ for the next-nearest-neighbor ions. For the potential $V(\mathbf{r}_m)$ we take $V_A(\mathbf{r}_m)$ or $V_B(\mathbf{r}_m)$. The sign $v_{ml} = \pm 1$ is plus (minus) for the next-nearest-neighbor hopping path via the common neighbor ion that turns counterclockwise (clockwise).

In Eq. (8) p_{ml} is the Peierls phase $p_{ml} = e^{i\frac{e}{\hbar} \int_{\mathbf{r}_m}^{\mathbf{r}_l} \vec{A} \cdot d\vec{l}}$, where $\vec{A} = (0, Bx, 0)$ is the vector potential, and B is the value of the magnetic field that is oriented perpendicular to the silicene plane. The last term in Eq. (8) is the spin Zeeman term with the Landé factor $g = 2$, and Bohr magneton μ_B .

2. Initial condition and the time-stepping

In the calculations to follow for the initial condition we use the solution of the continuum Hamiltonian [Eq. (2)] and localize the packet along the band inversion using an envelope of form $\frac{1}{1 + \frac{(y-y_0)^2}{D^2}}$, with $D = 80$ nm and y_0 that sets the center of the packet. We set the valley momentum with a plane wave and the K or K' coordinates. Accordingly, for the atoms of the A sublattice we set as the initial condition

$$\psi(\mathbf{r}_m^A, t = 0) = \exp[i(\mathbf{K}_\eta + \mathbf{k}_y) \cdot \mathbf{r}_m^A] \chi(y_m^A), \quad (9)$$

where $\mathbf{k}_y = (0, k_y, 0)$ is the wave vector of the packet calculated with respect to the valley center, and Ψ_A is given by Eq. (6). For the atoms on the B sublattice we take

$$\psi(\mathbf{r}_m^B, t = 0) = i\eta \exp[i(\mathbf{K}_\eta + \mathbf{k}_y) \cdot \mathbf{r}_m^B] \chi(y_m^B), \quad (10)$$

where $\chi(y) = \frac{\Psi_A(y)}{1 + \frac{(y-y_0)^2}{D^2}}$. We set $k_y = 0$ unless stated otherwise.

We solve the Schrödinger equation on the atomic lattice $i\hbar \frac{\partial \psi}{\partial t} = H\psi$, using the time step of $dt = 10$ atomic units or $dt = 2.418 \times 10^{-4}$ ps. The wave function at the first step is calculated with the implicit Crank-Nicolson scheme $\psi(dt) = \psi(0) + \frac{dt}{2i\hbar} H_{TB} [\psi(0) + \psi(dt)]$. The subsequent time steps are calculated with the explicit Askar-Cakmack scheme $\psi(t + dt) = \psi(t - dt) + \frac{2dt}{i\hbar} H_{TB} \psi(t)$. In presence of the external magnetic field the eigenstates of (3,4) need to be calculated numerically [63]. However, for the discussed range of the magnetic field ($B < 1$ T) and the applied narrow flip area ($\lambda = 4$ nm) no significant difference between the numerical eigenstates and formula of Eq. (6) used for the initial condition were found in the wave packet evolution.

III. RESULTS

A. Wave packet motion

We first consider a square flake $(x, y) \in [-300 \text{ nm}, 300 \text{ nm}] \times [-300 \text{ nm}, 300 \text{ nm}]$ with a zigzag

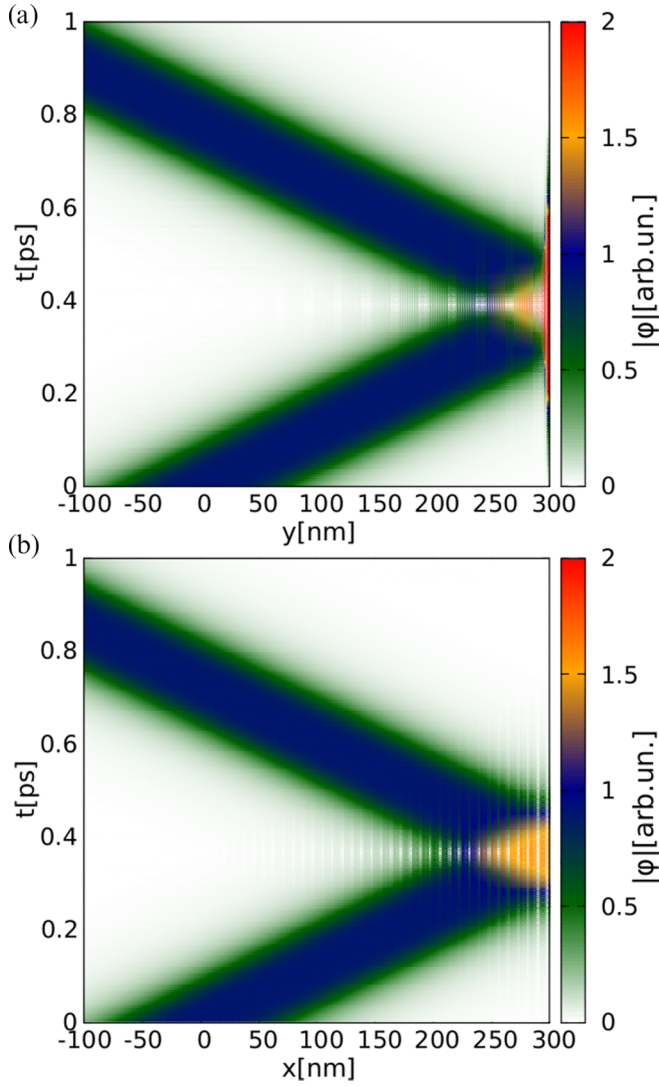


FIG. 2. Time evolution of the absolute value of the electron packet ($|\phi|$) backscattered by the zigzag (a) and armchair (b) edge of the flake. The square flake has a zigzag edge at $y = 300$ nm (a) and an armchair edge at $x = 300$ nm (b). The plots show the absolute value of the wave function at the inversion of the energy band that is introduced at $x = 0$ (a) and at $y = 0$ (b). For the zigzag edge the wave packet is temporarily localized at the edge. The vertical fringes observed at the backscattering result from the superposition of the incoming and outgoing waves from the opposite valleys K and K' .

edge at $y = \pm 300$ nm and armchair edge at $x = \pm 300$ nm. The packet is set in the K' valley ($\eta = -1$) to make it move upwards [to increasing y values—see Fig. 1(b)]. Figure 2(a) shows the cross section of the packet along the $x = 0$ line. The packet indeed moves up in a stable form until it reaches the zigzag edge of the flake.

The same result—as long as the packets does not reach the edge—is obtained for the solution of the time dynamics with the continuum Hamiltonian [by Eq. (2)]. The absence of Zitterbewegung [41–44] for the wave packet that follows the Dirac equation calls for a comment. The velocity operator is obtained as $\hat{v}_y = \frac{1}{\hbar} \frac{\partial H_\eta}{\partial k_y} = -\eta \tau_y v_f$ [42]. For the Dirac equation this operator does not commute with the Hamiltonian

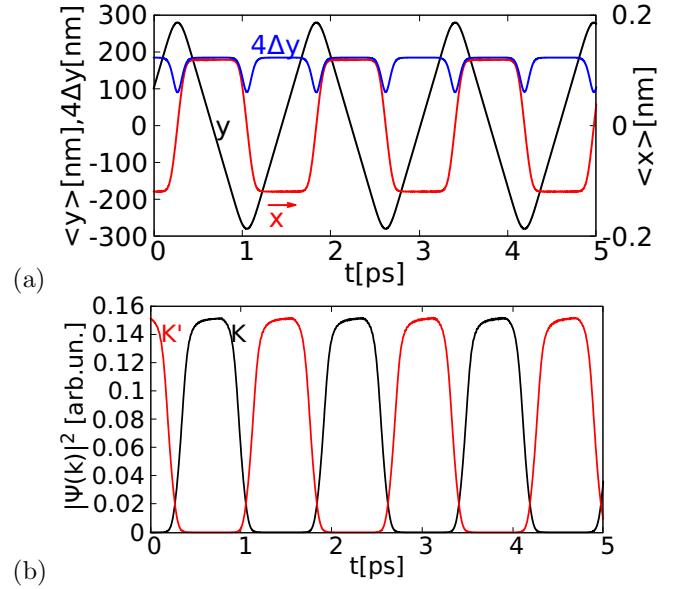


FIG. 3. (a) The average position in the y (black line, left axis) direction for the wave packet scattered by the armchair edge of the flake. The spread of the wave packet $\sqrt{\langle (y - \langle y \rangle)^2 \rangle}$ multiplied by 4 (blue line, left axis), and the average position at the x axis (right axis, red line). The variation of $\langle x \rangle$ are due to the spin-orbit coupling and the valley transitions that follow the backscattering by the edge [see. Eq.(6)]. The electron spin is set at $\sigma_z = +1$. The parameters of the system are the same as in Fig. 2(a), only the packet is started with the initial average position at $y_0 = 100$ nm. (b) The Fourier transform of the packet calculated for the K' (red) and K valley (black).

$[H_\eta, v_y] \neq 0$ which is usually invoked in the interpretation of the trembling motion [42]. However, the wave function localized at the zero line that follows the specific form used in Sec. II A $\Psi = (\Psi_A, i\Psi_A)^T$ happens to be an eigenfunction of the \hat{v}_y operator, with the eigenvalue $v_y = -\eta v_f$. By the Ehrenfest theorem for we have $\frac{d}{dt} \langle \Psi | \hat{v}_y | \Psi \rangle = \frac{1}{i\hbar} \langle \Psi | [\hat{v}_y H - H \hat{v}_y] | \Psi \rangle = \frac{1}{i\hbar} (\langle H \hat{v}_y \Psi | \Psi \rangle - \langle \Psi | H \hat{v}_y \Psi \rangle) = \frac{1}{i\hbar} (-\eta v_f \langle H \Psi | \Psi \rangle + \eta v_f \langle \Psi | H \Psi \rangle) = 0$, hence the constant velocity of the packet.

B. Backscattering by the flake edge

The zigzag edge of the crystal supports edge localized states. The incident packet couples to these states and in Fig. 2(a) we find formation of a high peak of the absolute value of the wave function (see the red region at the right edge of the plot for $t \simeq 0.4$ ps). The packet is backscattered and moves to the left with a shape restored to its original form, only in the opposite direction.

The average position $\langle y \rangle$, $\langle x \rangle$, and the size of the packet along the junction $\Delta y \equiv \sqrt{\langle (y - \langle y \rangle)^2 \rangle}$ is plotted in Fig. 3(a). The system is the same as in Fig. 2(a) only the packet is started at $y_0 = 100$ nm. In Fig. 3(b) we additionally plot the square of the absolute value of the Fourier transform of the wave packet calculated for K and K' valleys,

$$\psi(\mathbf{k}, t) = \frac{1}{2\pi} \int \psi(x, y, t) \exp(-i\mathbf{k} \cdot \mathbf{r}) d\mathbf{r}, \quad (11)$$

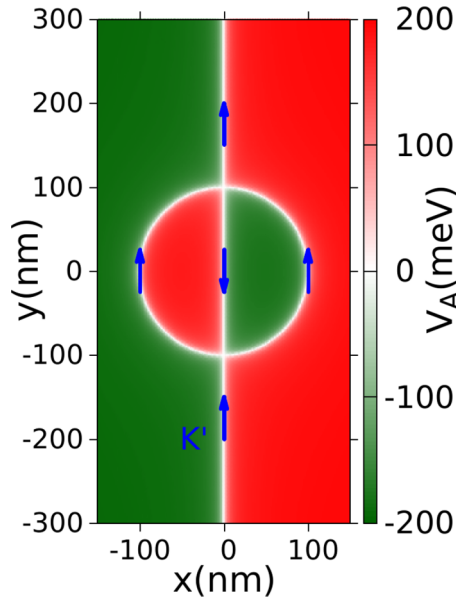


FIG. 4. The potential at the A sublattice for a quantum ring of radius 100 nm. The potential at the B sublattice is assumed opposite. The arrows indicate the orientation of the K' currents. The currents in the K valley flow in the opposite direction.

for $\mathbf{k} = \mathbf{K}_{-1}$ (i.e., the K' valley) and $\mathbf{k} = \mathbf{K}_1$ (K valley). We find that as the packet reaches the edge of the flake it is scattered to the other valley that makes it travel in the opposite direction. In Fig. 3(a) we can also see that the average $\langle x \rangle$ oscillates with a small magnitude which results from the valley flips at the backscattering by the edge which changes the sign of the exponent with t_{SO} in the wave function (σ_z is set to 1).

We find that the restoration of the chiral packet upon scattering is observed for both the armchair and the zigzag termination of the flake. For backscattering by the armchair edge we rotated the potential within the flake by $-\pi/2$ angle. The packet which is still started in the K' valley moves toward larger x values until it reaches the edge [Fig. 2(b)]. Here no peak of the wave function at the edge is observed since the armchair termination does not support the edge localized states [65].

C. Quantum ring

A form of a quantum ring with the chiral wave guides for the electron flow can be defined with an engineering of the electric field. For that purpose one needs a local inversion of the electric field which requires additional top and bottom gates in the system. Here we consider a circular area of radius R , and set the model potential at the A sublattice to

$$V_A = \frac{4V_g}{\pi^2} \arctan\left(\frac{r-R}{\lambda}\right) \arctan\left(\frac{x}{\lambda}\right), \quad (12)$$

where $R = 100$ nm is the circle radius with the center at the origin and $r = \sqrt{x^2 + y^2}$ is the distance from the origin. The potential at the A sublattice is plotted in Fig. 4. As above we take $V_B(\mathbf{r}) = -V_A(\mathbf{r})$. Figure 4 shows also the direction of the flow for currents in the K' valley—with the negative

(positive) potential at left (right) side of the current flow. When the line of $V_A = 0$ meets the ring at $y = -100$ nm the K' current can go to either the left or the right arm of the ring. This potential profile introduces a beam splitter for the electron wave packet in this way. The central bar of the ring is inaccessible for the K' current going up.

In quantum rings [49] Aharonov-Bohm [50] oscillations of coherent conductance are observed that in the Landauer-Büttiker [66] approach are explained as due to variation of the electron transfer probability across the ring with phase shifts accumulated from the vector potential of the magnetic field. In the present system the electron backscattering from the ring is prohibited by the topological protection of the valley current, so the transfer probability of the chiral wave packet is 1 for any magnetic field. However, we find that the time that the electron spends within the ring changes due to the phase shifts introduced by the vector potential.

In this section and in the rest of the paper we neglect the intrinsic spin-orbit coupling ($t_{SO} = 0$) that introduces a weak asymmetry in the electron injection to the ring due to the spin-valley dependent shift off the zero line [cf. Fig. 3(a) and Eq. (6)]. The calculations for the quantum ring require long leads to prevent return of the packet to the scattering area upon reflection from the edge of the crystal. For long wave packets the entire computational box is taken long up to $6 \mu\text{m}$. Systems these long are treated with the scaling method of Ref. [67] for which the crystal constant is scaled as $a_s = as_f$ with the hopping parameter $t_s = t/s_f$. In Hamiltonian Eq. (8) t_s replaces t , and a_s replaces a while the Si ions are generated in the computational box. We use the scaling factor $s_f = 3$ or 4 in the calculations for silicene below.

Figure 5(a) shows the snapshots of the simulation of the packet transfer across the ring for $B = 0$. For $t = 0$ the packet is started 350 nm below the center of the ring of radius 100 nm. The snapshots taken at 0.204 and 0.325 ps show that the packet is split into two parts at the entrance to the ring. In both the left and right arms of the ring the K' current moves up leaving the negative potential at the A sublattice at the left-hand side [see Fig. 4]. The split packets meet at the exit of the ring [$t = 0.568$ ps and $t = 0.689$ ps] with the same phase and the packet of its original size is restored [$t = 0.810$ ps].

Figure 6(a) shows the parts of the packet before (“b4,” black lines) the ring, within (“in,” blue lines), as well as the transferred part (“passed,” red lines) as a function of time. The results for $B = 0$ that correspond to Fig. 5(a) are plotted with the solid lines. For $t = 0.75$ ps the entire packet is transferred above the ring.

Below we denote the magnetic field flux threading the ring by $\Phi \equiv B\pi R^2$. For $R = 100$ nm the flux is equal to the flux quantum $\Phi_0 = \frac{h}{e}$ when $B = 0.13167$ T. In Fig. 5(b) we plotted the snapshots of the simulation for $B = 0.066$ T, which corresponds to $\Phi = \Phi_0/2$. The parts of the packet that meet at the exit ($t = 0.6$ ps) acquire a relative π phase due to the Aharonov-Bohm effect. A node of the wave function is formed at the exit to the upper channel. A nondestructive interference is observed within the area below the exit from the ring, which directs the packet to the internal bar within the ring ($t = 0.72$ ps), i.e., to the only path where the K' current can go for the exit to the upper channel blocked by

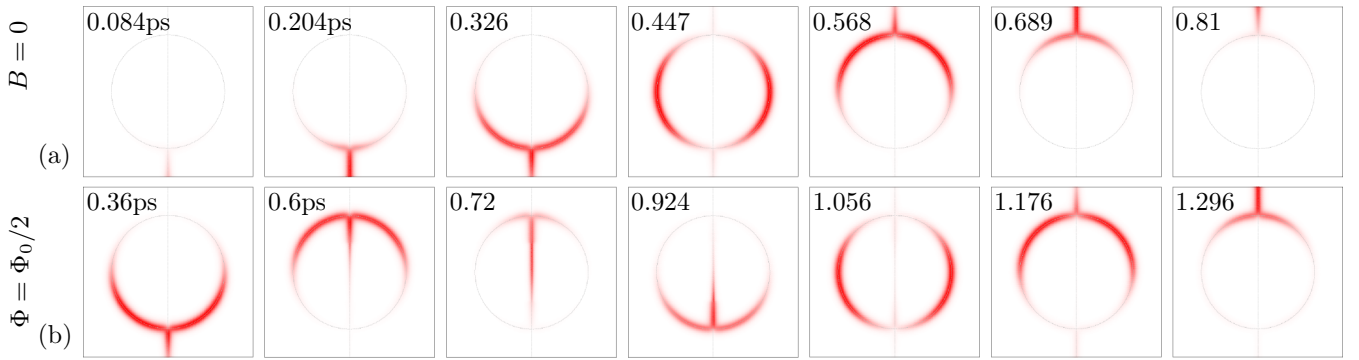


FIG. 5. The snapshots of the time evolution of the wave packet for $B = 0$ (a) and $B = 0.066$ T (b), which corresponds to the magnetic field flux across the ring of radius $R = 100$ nm $\Phi = B\pi R^2$ equal to half the flux quantum $\Phi_0 = h/e$, $\Phi = \Phi_0/2$. The time from the start of the simulation is given in picoseconds in the frames.

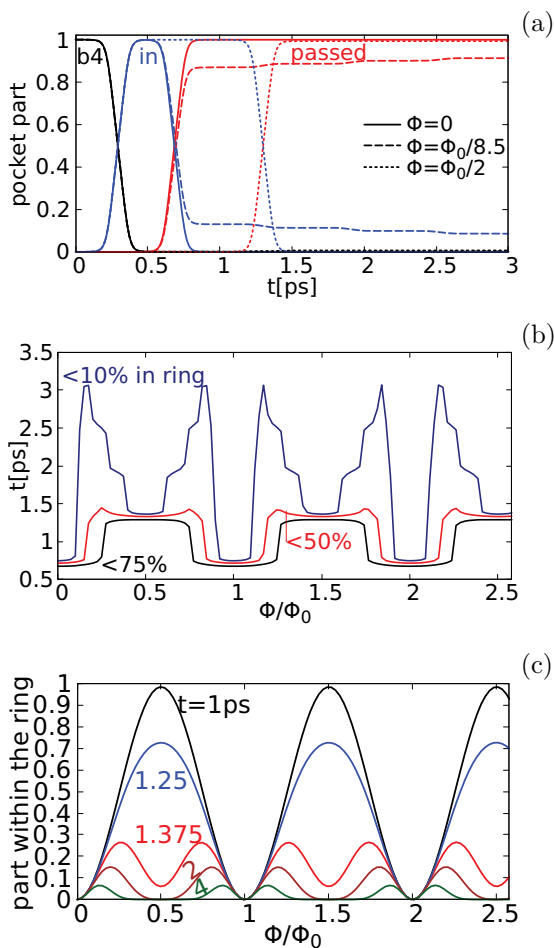


FIG. 6. (a) The part of the wave packet before the ring (black lines), inside the ring (blue lines), and above the ring (red lines) for zero magnetic field (solid lines), half of the flux quantum ($B = 0.066$ T), and the magnetic field corresponding to the flux equal to $\Phi_0/8.5$ ($B = 0.0155$ T). (b) The time at which less than 10% (blue line), 50% (red line), and less than 75% of the electron density stays within the ring as a function of the magnetic field flux through the ring of radius $R = 100$ nm. Local extrema of the times are found even and odd multiples of $\Phi_0/2$. (c) The part of the wave packet inside the ring for the selected moments in time from the start of the simulation.

the Aharonov-Bohm effect. The bar is transparent for the K' current going down [Fig. 4]. The packet is split again to the left and right arms of the ring at 0.924 ps. After the second round the parts of the packet meet in phase 2π at the exit and the packet smoothly leaves the ring [$t = 1.176$ ps, $t = 1.296$ ps].

In Fig. 6(a) the results for half the flux quantum are plotted with the dotted line. The packet is transferred to the exit with a delay but completely and in a single move. For comparison in Fig. 6(a) the results for the magnetic field of 0.0155 T which corresponds to $\Phi_0/8.5$ are plotted with the dashed lines. Here a part of the packet passes to the exit as fast as for $B = 0$, but due to a phase difference at the exit a part of the packet stays inside the ring and leaves it in portions at subsequent rounds, which produces the steps in the dashed lines in Fig. 6(a).

In Fig. 6(b) we plotted the moments in time for which less than 75%, less than 50% and less than 10% stays within the ring as a function of the external magnetic field. The plot is periodic with Φ_0 . The ring is emptied the fastest for the integer and half quanta. The result of Fig. 6(a) for $\Phi = \Phi_0/8.5$ (or $B = 0.0155$ T) corresponds to a local maximum of the time for which more than 10% of the packet stays within the ring. Finally, Fig. 6(c) shows the part of the packet contained within the ring for a fixed moment in time as a function of the magnetic field. For $t = 1$ ps and 1.25 ps the ring-confined part is locally maximal for the magnetic field corresponding to odd multiples of half the flux quantum. For longer times these maxima are turned into minima due to compensation of the phase difference after the second round of electron circulation [Fig. 5(b)] within the ring.

D. Intervalley scattering and conductance oscillations

For the potential profile plotted in Fig. 4 the transfer probability can fall below 1 only provided that a intervalley transition is present within the ring. The intervalley scattering is introduced by potential variation that is short on the atomic scale. For the modeling we introduced a point potential defect of a Lorentzian form

$$V_d(\mathbf{r}) = \frac{V_g}{1 + (\mathbf{r} - \mathbf{r}_d)^2/l^2}, \quad (13)$$

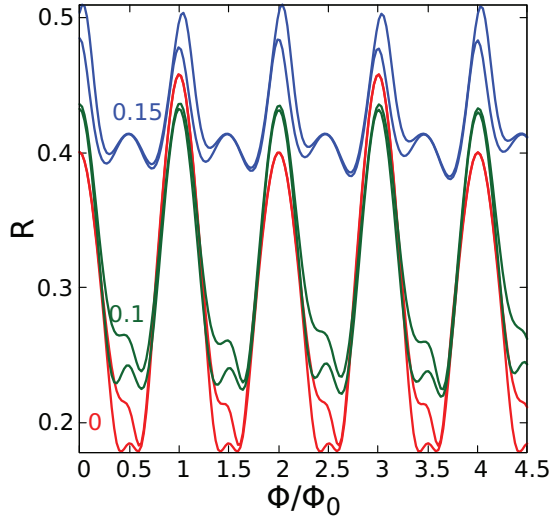


FIG. 7. The backscattering probability for a sharp perturbation to the potential given by Eq. (13) as a function of the magnetic field flux threading the ring of radius $R = 100$ nm. The red, green, and blue lines correspond to $k_y = 0, 0.1/\text{nm}$, and $0.15/\text{nm}$, respectively. For each value of k_y , two lines are plotted: the lower and upper bound to the backscattering probability. The spacing between these two lines is given by the probability density localized within the ring at the end of the simulation (6.1 ps from the start).

where $\mathbf{r}_d = (R, 0, 0)$, and $V_g = 7.2/s_f^2$ eV and $l = 12a = 4.7$ nm. In the scaling approach [67] the smooth potential that changes slowly on the atomic scale, in particular, the one given by Eqs. (1) and (12) stays invariant with s_f . For the abrupt short-range defect potential we found that scaling of V_g with s_f is necessary to keep the same effectiveness of the intervalley scattering. The defect potential V_d enters with the same sign to potential on both sublattices, as $V_A + V_d$ on sublattice A and $V_B + V_d = -V_A + V_d$ on sublattice B.

In presence of the defect, the results start to change significantly with k_y . The backscattering probability R as a function of the external field is given in Fig. 7 for $k_y = 0, 0.1/\text{nm}$, and $0.15/\text{nm}$. For each value of k_y , two lines are plotted, which are the minimal and maximal bound for the backscattering probability. The difference between the two is determined by the part of the electron packet that stays within the ring at the end of the simulation (6.1 ps). R as a function of B is approximately periodic with the period of flux quantum threading

the ring. The behavior of the electron packet is displayed in Fig. 8 for $B = 0$ and $k_y = 0.1/\text{nm}$. The packet is incident in the K' valley. For $t = 0.508$ ps we spot the scattering center near \mathbf{r}_d . A part of the packet passes across the defect moving still in K' valley, and a larger part is backscattered and move in the direction which is only allowed for the K valley. For $t = 0.628$ ps the K current reaches the entrance to the ring, a part of it is backscattered to the input channel, and another goes up along the bar. The electron packets of opposite valley meet within the bar for $t = 0.749$ ps and 0.87 ps. For $t = 0.991$ ps we can see recycling of currents for both the valleys: the K valley current cannot pass to the output channel and the K' one to the input channel. The opposite valley currents meet again, this time in the arms of the ring for $t = 1.11$ ps. For $t = 1.47$ ps the packet distribution is similar to $t = 0.87$ ps, only a smaller portion of the electron packet is still present within the ring.

E. The limit of long wave packets

The wave packet dynamics in the limit of a large size of the packet should approach the conditions of the stationary electron flow. To study the limit of a plane incident wave we consider a Gaussian envelope of the packet, i.e., in the initial condition given by Eqs. (9) and (10) we set $\chi = \exp[-(y - y_0)^2/4\sigma^2]/(2\pi\sigma^2)^{1/4}$. The Fourier transform of the packet produces the probability density with the standard deviation of $\sigma_k = \frac{1}{2\sigma}$ in the wave vector space.

We solve the time evolution and integrate the parts of the packet in the left and right arms of the ring and in the center bar over time as the packet transfers the ring. In Fig. 9 we plot the results for increasing length of the packet in the initial condition. The results for $\sigma = 30$ nm and $\sigma = 60$ nm are nearly identical. The packet passes equally through the left and right arms of the ring. The integrals in Figs. 9(a) and 9(b) are periodic functions of the magnetic field with the quantum of the flux threading the ring of radius $R = 100$ nm, as above. An asymmetry of the electron transfer across the arms appears for $\sigma = 120$ nm [Fig. 9(c)] and becomes very strong for $\sigma = 240$ nm [Fig. 9(d)]. Moreover, as the result of this asymmetry, the period of the integrals as functions of the magnetic flux threading the ring of radius R doubles and becomes equal to $2\Phi_0$. For explanation of this effect the solution of the stationary scattering problem of the next subsection is helpful.

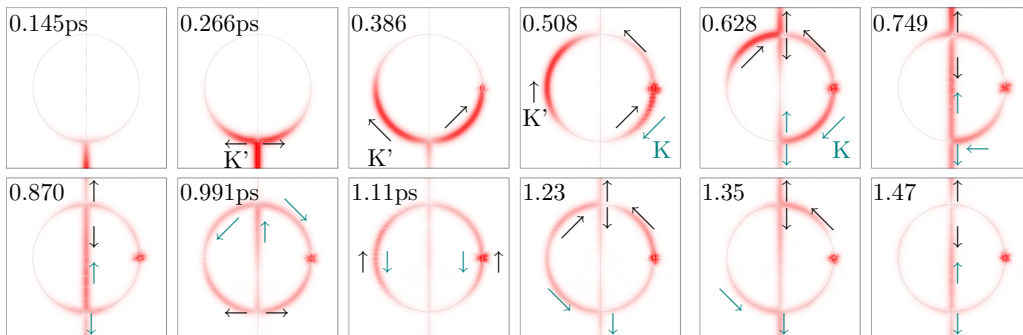


FIG. 8. Snapshots of the electron density for $B = 0$, $k_y = 0.1/\text{nm}$ [the green lines in Fig. 7(a)]. The blue (green) arrows indicate the motion of the parts of the packet moving in the K (K') valley. The time from the start of the simulation is given in picoseconds in the frames.

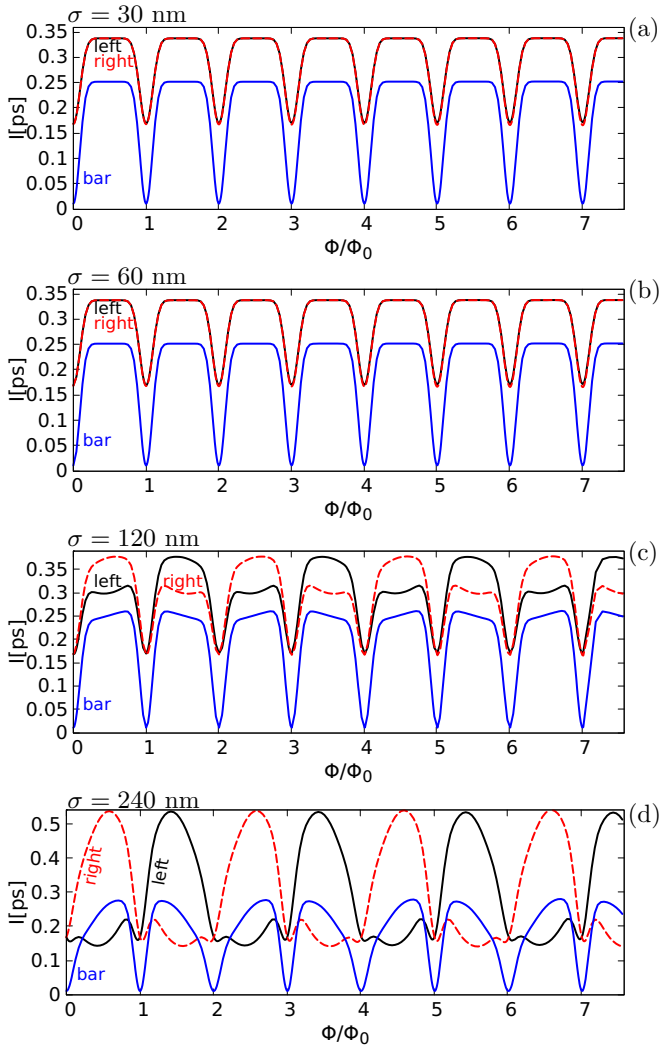


FIG. 9. Probability density in the left (red dashed line) and right (black line) arms of the ring and in the central bar (blue line) integrated over time, for a Gaussian envelope of the wave packet in the initial condition $\exp[-(y - y_0)^2/4\sigma^2]$, with σ given in the figure. The wave vector applied in the initial condition is $k_y = 0.01/\text{nm}$.

F. Stationary electron flow

We solve the standard stationary quantum scattering problem for the Fermi level electron using the wave function matching technique [68] for the atomistic tight binding Hamiltonian. We set $E_F = 6.4$ meV for which the Fermi wave vector is displaced by $k_y = 0.01/\text{nm}$ from the K' Dirac point at $B = 0$. The integral over the scattering density in space is plotted in Fig. 10(a). The result corresponds very well with Fig. 9(d), only the features are more abrupt in the stationary case, which is due to the presence of a finite range of k_y in the wave packet dynamics. The period of integrals is $2\Phi_0$.

Figures 10(b)–10(d) show the scattering density for $\Phi = 0.91\Phi_0$, $0.99\Phi_0$, and $1.06\Phi_0$, respectively. For $0.99\Phi_0$ [Fig. 10(c)] the parts of the electron density passing through both the arms of the ring meet in phase at the exit to the ring, and the electron wave function does not enter the central bar. However, for slightly different magnetic field [Figs. 10(b) and 10(d)] a phase difference appears, the part of the wave

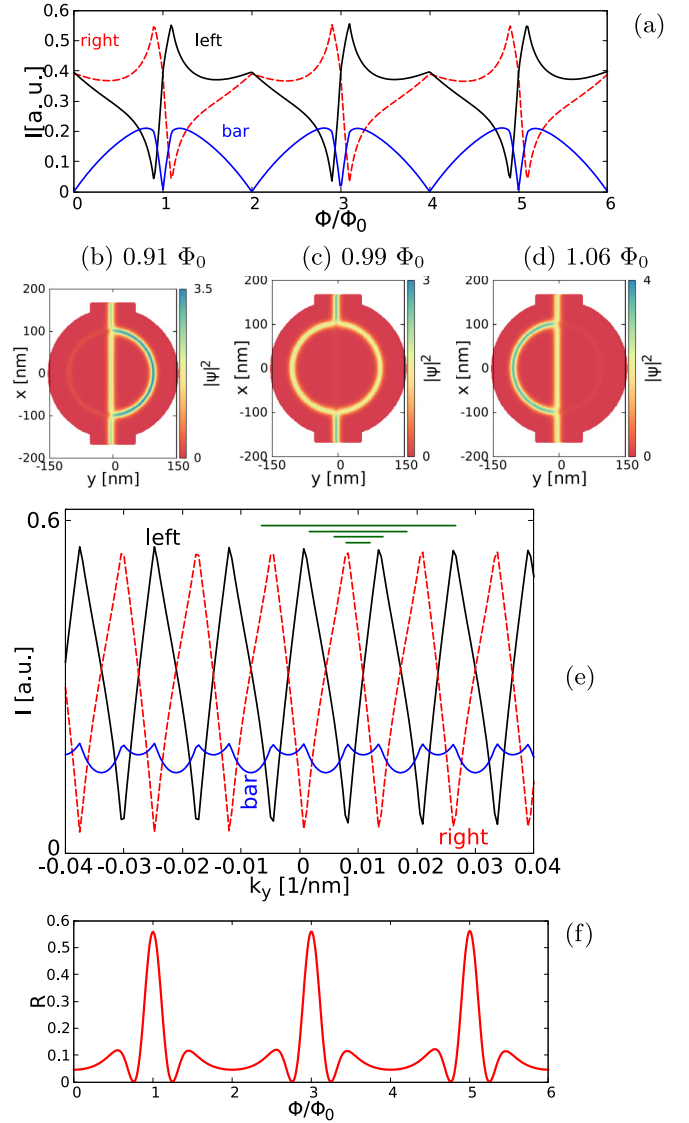


FIG. 10. Solutions of the stationary scattering problem for $E_F = 6.4$ meV, which corresponds to the wave vector $k_y = 0.01/\text{nm}$ as calculated with respect to the K' valley. (a) Scattering density integrated over the left (red dashed line), the right (black line) arm of the ring, and in the central bar (blue line). (b–d) The scattering density for $B = 0.12, 0.13, 0.14$ T, that correspond to the flux of the magnetic field threading the ring of radius 100 nm $\Phi = 0.91\Phi_0, 0.99\Phi_0$, and $1.06\Phi_0$, respectively. (e) Same as (a) only as a function of k_y for $B = 0.075$ T ($\Phi = 0.57\Phi_0$). The horizontal bars show the segments $[k_y - \sigma_k, k_y + \sigma_k]$ with the standard deviation of the Gaussian packet $\sigma_k = \frac{1}{2\sigma}$ for $\sigma = 30, 60, 120$, and 240 nm, from top to bottom. (f) Backscattering probability obtained for the defect potential given by Eq. (13).

function is injected to the central bar from above, and the interference within the ring promotes right or left arm of the ring. In the extreme conditions of Figs. 10(b) and 10(d) the electron circulates around a *half* of the entire ring, which is the origin of the period doubling of the period on the flux scale, as now the area for the magnetic field flux is halved.

In the time-dependent dynamics for short packets the injection to both the arms of the ring is nearly ideally symmetric.

Figure 10(e) gives the integrals for the stationary flow for $\Phi = 0.57\Phi_0$ (i.e., $B = 0.075$ T) as a function of k_y . The scattering density switches very fast from the left to the right arms of the ring. The horizontal bars at the top of the Figure show the segments of k_y from $0.01 \frac{1}{\text{nm}} \pm \sigma_k = 0.01 \frac{1}{\text{nm}} \pm \frac{1}{2\sigma}$, for $\sigma = 30, 60, 120,$ and 240 nm (from top to bottom). Only for large σ the asymmetry survives averaging over k_y range contained within the packet, hence the symmetric transfer for shorter packets.

Figure 10(f) shows the backscattering probability R for the ring with the defect given by Eq. (13). The conductance $G = (1 - R) \frac{e^2}{h}$ has a period of $2\Phi_0$ in terms of the flux threading the entire ring, or the period of the oscillations corresponds to the flux quantum threading half of the ring in consistency with the period of the scattering density integrals of Fig. 10(a).

G. Quantum rings defined by zero lines in bilayer graphene

Qualitatively similar results for the transfer across the quantum rings defined by the zero lines of the symmetry-breaking electric field are found for the bilayer graphene.

For bilayer graphene we use the atomistic tight-binding Hamiltonian spanned by p_z orbitals,

$$H = \sum_{\langle i,j \rangle} (t_{ij} c_i^\dagger c_j + \text{H.c.}) + \sum_i V(\mathbf{r}_i) c_i^\dagger c_i, \quad (14)$$

where $V(\mathbf{r}_i)$ is the external potential at the i th site at position \mathbf{r}_i , and in the first term we sum over the nearest neighbors. We use the tight-binding parametrization of Bernal stacked layers [69], with $t_{ij} = -3.12$ eV for the nearest neighbors within the same layer. For the interlayer coupling, we take $t_{ij} = -0.377$ eV for the A-B dimers, $t_{ij} = -0.29$ eV for skew interlayer hoppings [69] between atoms of the same sublattice (A-A or B-B type), and $t_{ij} = 0.12$ eV for skew interlayer hopping between atoms of different sublattices. The orbital effects of the magnetic field are introduced by Peierls phase, as in Sec. II B 1.

For simulation of the ring, we assume potential of the form given by Eq. (12) on the upper sublattice and an opposite potential on the lower sublattice [see Fig. 11(a)]. We set $V_g = 0.2$ eV, $\lambda = 4$ nm as above, but the radius of the ring is taken equal to $R = 50$ nm. The magnetic field period corresponding to the flux quantum threading the circle of this radius is 0.53 T.

The dispersion relation for armchair nanoribbon is displayed in Fig. 11(b). For calculations we take the the Fermi energy is $E_F = 0.1$ eV. For bilayer graphene we have two energy bands instead of the single one moving up the ribbon towards the ring. The integrals of the scattering density are plotted in Fig. 11(c) and display the periodicity with Φ period of $2\Phi_0$, as found above for silicene.

To produce the backscattering we removed an atom of the upper graphene layer from the center of the right arm. We selected an atom that does not form a vertical dimer with the lower layer. The backscattering probability—the sum of probabilities for each of the incident subbands—is given in Fig. 11(d) and display the periodicity corresponding to the flux through half the ring, as found above for silicene.

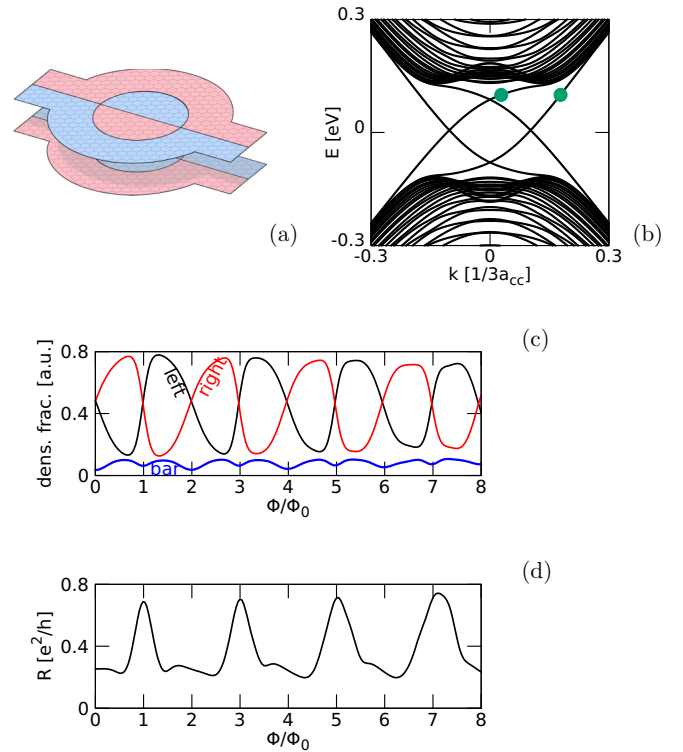


FIG. 11. (a) Schematics of the potential on the upper and lower layers of bilayer Bernal stacked graphene. Blue and red colors correspond to opposite sign of the potential. We consider an armchair nanoribbon of width $W = 49.2$ nm, with 1604 atoms in the elementary cell (on both layers). The zero line forms the ring of radius $R = 50$ nm. The computational box in the ring area covers an area of radius 74.5 nm. (b) The dispersion relation for the armchair nanoribbon feeding the current to the ring at $B = 0$. The dots indicate the Fermi wave vectors at the bands with positive velocity for $E_F = 0.1$ eV. a_{cc} is the nearest-neighbor distance for graphene. (c) Integral of the scattering density in the left and right arms of the ring and in the bar for $E_F = 0.1$ eV. (d) Backscattering probability for a vacancy: a carbon atom removed from the center of the right arm from a position that does not form a vertical dimer with the bottom layer.

IV. SUMMARY

We studied the dynamics of electron wave packets in buckled silicene in inhomogeneous vertical electric field that breaks the symmetry between the sublattices using an atomistic tight-binding approach. We have demonstrated that the line of the electric field flip in silicene supports a smooth untrembling motion of unspreading wave packets that are topologically protected from backscattering. We proposed a form of a quantum ring that uses branching of the zero line to split the wave packets and to make them interfere again. The ring stores the packet for a finite time that can be controlled with the external magnetic field. For short wave packets the time spent by the electron in the left and right arms of the ring is a periodic function of the flux with the period of the flux quantum threading the ring. We found that for long packets, close to the plane waves, the electron transport across the rings becomes asymmetrical with an imbalance of the electron transfer across the left and right halves of the ring. In consequence the period of oscillations in terms of the magnetic field

flux across the ring is doubled. This result is reproduced by stationary scattering calculations. We demonstrated that the same effect is found for rings defined in bilayer graphene. The point defects produce backscattering probability that has a period of the flux quantum threading the ring for short packets. For long packets and in the stationary transport the period of the backscattering probability is doubled.

ACKNOWLEDGMENTS

The results of Sec. III F were obtained by B.R. (stationary transport silicene), who was supported by the Pol-

ish Government budget for science 2017–2021 within the Diamentowy Grant project (Grant No. 0045/DIA/2017/46). The results of Sec. III G were calculated by A.M.-K. (stationary transport bilayer graphene), who was supported by National Science Centre (NCN) according to decision DEC-2015/17/B/ST3/01161. The rest of the results were provided by B.S., who was supported by the National Science Centre (NCN) according to decision DEC-2016/23/B/ST3/00821. B.R. acknowledges the support of EU PhD Project POWER.03.02.00- 00-I004/16. The calculations were performed on PL-Grid Infrastructure at ACK Cyfronet AGH.

- [1] A. H. Castro Neto, F. Guinea, N. M. R. Peres, K. S. Novoselov, and A. K. Geim, *Rev. Mod. Phys.* **81**, 109 (2009).
- [2] A. Molle, J. Goldberger, M. Houssa, Y. Xu, S.-C. Zhang, and D. Akinwande, *Nat. Mater.* **16**, 163 (2017).
- [3] B. Aufray, A. Kara, S. Vizzini, H. Oughaddou, C. Léandri, B. Ealet, and G. Le Lay, *Appl. Phys. Lett.* **96**, 183102 (2010).
- [4] Cheng-Cheng Liu, Wanxiang Feng, and Yugui Yao, *Phys. Rev. Lett.* **107**, 076802 (2011).
- [5] S. Cahangirov, M. Topsakal, E. Akturk, H. Sahin, and S. Ciraci, *Phys. Rev. Lett.* **102**, 236804 (2009).
- [6] Y. Xu, B. Yan, H.-J. Zhang, J. Wang, G. Xu, P. Tang, W. Duan, and S.-C. Zhang, *Phys. Rev. Lett.* **111**, 136804 (2013).
- [7] K. F. Mak, C. Lee, J. Hone, J. Shan, and T. F. Heinz, *Phys. Rev. Lett.* **105**, 136805 (2010).
- [8] F. Reis, G. Li, L. Dudy, M. Bauernfeind, S. Glass, W. Hanke, R. Thomale, J. Schaefer, and R. Claessen, *Science* **357**, 287 (2017).
- [9] K. Wakabayashi, Y. Takane, M. Yamamoto, and M. Sigrist, *New J. Phys.* **11**, 095016 (2009).
- [10] K. Nakada, M. Fujita, G. Dresselhaus, and M. S. Dresselhaus, *Phys. Rev. B* **54**, 17954 (1996).
- [11] K. Wakabayashi, *Phys. Rev. B* **64**, 125428 (2001).
- [12] N. M. R. Peres, A. H. Castro Neto, and F. Guinea, *Phys. Rev. B* **73**, 195411 (2006).
- [13] M. I. Katsnelson, K. S. Novoselov, and A. K. Geim, *Nat. Phys.* **2**, 620 (2006).
- [14] A. Rycerz, J. Tworzydło, and C. W. J. Beenakker, *Nat. Phys.* **3**, 172 (2007).
- [15] J. R. Schaibley, H. Yu, G. Clark, P. Rivera, J. S. Ross, K. L. Seyler, W. Yao, and X. Xu, *Nat. Rev. Mat.* **1**, 16055 (2016).
- [16] X. Xu, W. Yao, D. Xiao, and T. F. Heinz, *Nat. Phys.* **10**, 343 (2014).
- [17] Z. Gong, G.-B. Liu, H. Yu, D. Xiao, X. Cui, X. Xu, and W. Yao, *Nat. Commun.* **4**, 2053 (2013).
- [18] Ivar Martin, Ya. M. Blanter, and A. F. Morpurgo, *Phys. Rev. Lett.* **100**, 036804 (2008).
- [19] W. Yao, S. A. Yang, and Q. Niu, *Phys. Rev. Lett.* **102**, 096801 (2009).
- [20] Edward McCann and Mikito Koshino, *Rep. Prog. Phys.* **76**, 056503 (2013).
- [21] T. Zhang, T.-T. Tang, C. Girit, Z. Hao, M. C. Martin, A. Zettl, M. F. Crommie, Y. R. Shen, and F. Wang, *Nature* **459**, 820 (2009).
- [22] Z. Qiao, J. Jung, Q. Niu, and A. H. MacDonald, *Nano Lett.* **11**, 3453 (2011).
- [23] M. Zarenia, J. M. Pereira, Jr., G. A. Farias, and F. M. Peeters, *Phys. Rev. B* **84**, 125451 (2011).
- [24] L. Ju, Z. Shi, N. Nair, Y. Lv, C. Jin, J. Velasco, Jr., C. Ojeda-Aristizabal, H. A. Bechtel, M. C. Martin, A. Zettl, J. Analytis, and F. Wang, *Nature* **520**, 650 (2015).
- [25] J. Li, K. Wang, K. J. McFaul, Z. Zern, Y. Ren, K. Watanabe, T. Taniguchi, Z. Qiao, and J. Zhu, *Nat. Nano.* **11**, 1060 (2016).
- [26] J. R. Williams, L. DiCarlo, and C. M. Marcus, *Science* **317**, 638 (2007); D. A. Abanin and L. S. Levitov, *ibid.* **317**, 641 (2007).
- [27] P. Rickhaus, P. Makk, M.-H. Liu, E. Tovari, M. Weiss, R. Maurand, K. Richter, and C. Schonenberger, *Nat. Commun.* **6**, 6470 (2015).
- [28] T. Taychatanapat, J. Y. Tan, Y. Yeo, K. Watanabe, T. Taniguchi, and B. Özyilmaz, *Nat. Commun.* **6**, 6093 (2015).
- [29] Y. Liu, R. P. Tiwari, M. Brada, C. Bruder, F. V. Kusmartsev, and E. J. Mele, *Phys. Rev. B* **92**, 235438 (2015).
- [30] S. Y. Zhou, G.-H. Gweon, A. V. Fedorov, P. N. First, W. A. de Heer, D.-H. Lee, F. Guinea, A. H. Castro Neto, and A. Lanzara, *Nat. Mater.* **6**, 770 (2007).
- [31] Z. Ni, Q. Liu, K. Tang, J. Zheng, J. Zhou, R. Qin, Z. Gao, D. Yu, and J. Lu, *Nano Lett.* **12**, 113 (2012).
- [32] N. D. Drummond, V. Zolyomi, and V. I. Fal'ko, *Phys. Rev. B* **85**, 075423 (2012).
- [33] M. Ezawa, *New J. Phys.* **14**, 033003 (2012).
- [34] S. Chowdhury and D. Jana, *Rep. Prog. Phys.* **79**, 126501 (2016).
- [35] M. Ezawa, E. Salomon, P. De Padova, D. Solonenko, P. Vogt, M. E. Davila, A. Molle, T. Angot, and G. Le Lay, *Riv. Nuovo Cimento* **41**, 175 (2018).
- [36] M. Ezawa, *Phys. Rev. Lett.* **109**, 055502 (2012).
- [37] B. Feng, Z. Ding, S. Meng, Y. Yao, X. He, P. Cheng, L. Chen, and K. Wu, *Nano Lett.* **12**, 3507 (2012).
- [38] P. Vogt, P. De Padova, C. Quaresima, J. Avila, E. Frantzeskakis, M. C. Asensio, A. Resta, B. Ealet, and G. Le Lay, *Phys. Rev. Lett.* **108**, 155501 (2012).
- [39] A. Fleurence, R. Friedlein, T. Ozaki, H. Kawai, Y. Wang, and Y. Yamada-Takamura, *Phys. Rev. Lett.* **108**, 245501 (2012).
- [40] L. Tao, E. Cinquanta, D. Chappé, C. Grazianetti, M. Fanciulli, M. Dubey, A. Molle, and D. Akinwande, *Nat. Nano.* **10**, 227 (2015).
- [41] A. O. Barut and A. J. Bracken, *Phys. Rev. D* **23**, 2454 (1981).
- [42] T. M. Rusin and W. Zawadzki, *Phys. Rev. B* **76**, 195439 (2007).

- [43] V. Ya. Demikhovskii, G. M. Maksimova, A. A. Perov, and E. V. Frolova, *Phys. Rev. A* **82**, 052115 (2010).
- [44] R. Gerritsma, G. Kirchmair, F. Zähringer, E. Solano, R. Blatt, and C. F. Roos, *Nature* **463**, 68 (2010).
- [45] E. Romera and F. de los Santos, *Phys. Rev. B* **80**, 165416 (2009).
- [46] S. Bednarek and B. Szafran, *Phys. Rev. Lett.* **101**, 216805 (2008); S. Bednarek, B. Szafran, R. J. Dudek, and K. Lis, *ibid.* **100**, 126805 (2008).
- [47] I. Bialynicki-Birula, M. Kalinski, and J. H. Eberly, *Phys. Rev. Lett.* **73**, 1777 (1994).
- [48] B. Wyker, S. Ye, F. B. Dunning, S. Yoshida, C. O. Reinhold, and J. Burgdörfer, *Phys. Rev. Lett.* **108**, 043001 (2012).
- [49] Edited by V. Fomin, *Physics of Quantum Rings* (Springer, Berlin, 2018).
- [50] Y. Aharonov and D. Bohm, *Phys. Rev.* **115**, 485 (1959).
- [51] P. Recher, B. Trauzettel, A. Rycerz, Ya. M. Blanter, C. W. J. Beenakker, and A. F. Morpurgo, *Phys. Rev. B* **76**, 235404 (2007).
- [52] D. Sticlet, B. Dora, and J. Cayssol, *Phys. Rev. B* **88**, 205401 (2013).
- [53] N. Bolivar, E. Medina, and B. Berche, *Phys. Rev. B* **89**, 125413 (2014).
- [54] S. Bellucci, A. A. Saharian, and A. Kh. Grigoryan, *Phys. Rev. D* **94**, 105007 (2016).
- [55] M. Saiz-Bretin, L. Medrano Sandonas, R. Gutierrez, G. Cuniberti, and F. Dominguez-Adame, *Phys. Rev. B* **99**, 165428 (2019).
- [56] M. Zarenia, J. M. Pereira, A. Chaves, F. M. Peeters, and G. A. Farias, *Phys. Rev. B* **81**, 045431 (2010).
- [57] L. Gioia, U. Zülicke, M. Governale, and R. Winkler, *Phys. Rev. B* **97**, 205421 (2018).
- [58] P. Michetti and P. Recher, *Phys. Rev. B* **83**, 125420 (2011).
- [59] A. Mreńca-Kolasińska, S. Heun, and B. Szafran, *Phys. Rev. B* **93**, 125411 (2016); A. Mreńca-Kolasińska and B. Szafran, *ibid.* **94**, 195315 (2016).
- [60] S. Soleimanikahnoj and I. Knezevic, *Phys. Rev. Appl.* **8**, 064021 (2017).
- [61] S. K. Banerjee, L. F. Register, E. Tutuc, D. Reddy, and A. H. MacDonald, *IEEE Electron Device Lett.* **30**, 158 (2009).
- [62] P. San-Jose, E. Prada, E. McCann, and H. Schomerus, *Phys. Rev. Lett.* **102**, 247204 (2009).
- [63] B. Szafran, A. Mreńca-Kolasińska, and D. Żebrowski, *Phys. Rev. B* **99**, 195406 (2019).
- [64] C.-C. Liu, H. Jiang, and Y. Yao, *Phys. Rev. B* **84**, 195430 (2011).
- [65] K. Wakabayashi, K. Sasaki, and T. Nakanishi, *Sci. Technol. Adv. Mater.* **11**, 054504 (2010).
- [66] M. Büttiker, *Phys. Rev. B* **38**, 9375 (1988).
- [67] M.-H. Liu, P. Rickhaus, P. Makk, E. Továri, R. Maurand, F. Tkatschenko, M. Weiss, C. Schonenberger, and K. Richter, *Phys. Rev. Lett.* **114**, 036601 (2015).
- [68] K. Kolasinski, B. Szafran, B. Brun, and H. Sellier, *Phys. Rev. B* **94**, 075301 (2016); B. Rzeszotarski and B. Szafran, *ibid.* **98**, 075417 (2018).
- [69] B. Partoens and F. M. Peeters, *Phys. Rev. B* **74**, 075404 (2006).